npj | climate and atmospheric science

Article

Published in partnership with CECCR at King Abdulaziz University

https://doi.org/10.1038/s41612-024-00797-w

The characterization, mechanism, predictability, and impacts of the unprecedented 2023 Southeast Asia heatwave

Check for updates

Yang Lyu[1,2], Jingyu Wang [2] ✉, Xiefei Zhi[1,3] ✉, Xianfeng Wang[4,5], Hugh Zhang[6], Yonggang Wen [7], Edward Park[2,4,5], Joshua Lee [6], Xia Wan[8], Shoupeng Zhu[9] & Duc Tran Dung[2,10]

In April and May 2023, Southeast Asia (SEA) encountered an exceptional heatwave. The Continental SEA was hardest hit, where all the countries broke their highest temperature records with measurements exceeding 42 °C, and Thailand set the region's new record of 49 °C. This study provides a comprehensive analysis of this event by investigating its spatiotemporal evolution, physical mechanisms, forecast performance, return period, and extensive impacts. The enhanced high-pressure influenced by tropical waves, moisture deficiency and strong land-atmosphere coupling are considered as the key drivers to this extreme heatwave event. The ECMWF exhibited limited forecast skills for the reduced soil moisture and failed to capture the land-atmosphere coupling, leading to a severe underestimation of the heatwave's intensity. Although the return period of this heatwave event is 129 years based on the rarity of temperature records, the combination of near-surface drying and soil moisture deficiency that triggered strong positive land-atmosphere feedback and rapid warming was extremely uncommon, with an occurrence probability of just 0.08%. These analyses underscore the exceptional nature of this unparalleled heatwave event and its underlying physical mechanisms, revealing its broad impacts, including significant health repercussions, a marked increase in wildfires, and diminished agricultural yields.

The world has witnessed a significant escalation in heatwaves in recent decades[1], leading to a surge in casualties across various regions. For example in Western Europe, the deadliest summer 2003 heatwave has caused ~70,000 excess deaths[2,3]. In July-August 2010, the heatwave-related death toll reached >10,000 in Russia[4]. During the 2021 Pacific Northwest heatwave, there have been 868 documented fatalities attributed to the event between 25 June and 2 July[5]. Recent studies have focused on the mid- and high-latitude regions undergoing unprecedented heatwave occurrences where the most pronounced surface warming trends were observed[6,7]. Nevertheless, Southeast Asia (SEA), traditionally known for its hot climate, has not received sufficient attention. Surrounded by the world's warmest oceans, SEA stands particularly vulnerable to heatwaves due to its dense population, diverse terrains, and underdeveloped economy[8,9]. Aligning with the increasing trends of heatwave exposure on a global scale, studies indicated that heatwaves over SEA are becoming more frequent, longer-lasting, and more intense as the consequences of global warming[10–13].

---

[1] Key Laboratory of Meteorology Disaster, Ministry of Education (KLME), Joint International Research Laboratory of Climate and Environment Change (ILCEC), Collaborative Innovation Center on Forecast and Evaluation of Meteorological Disasters (CIC-FEMD), Nanjing University of Information Science and Technology, Nanjing, China. [2] National Institute of Education (NIE), Nanyang Technological University (NTU), Singapore, Singapore. [3] WeatherOnline Institute of Meteorological Applications, Wuxi, China. [4] Earth Observatory of Singapore (EOS), Nanyang Technological University (NTU), Singapore, Singapore. [5] Asian School of the Environment (ASE), Nanyang Technological University (NTU), Singapore, Singapore. [6] Centre for Climate Research Singapore (CCRS), Singapore, Singapore. [7] College of Computing and Data Science (CCDS), Nanyang Technological University (NTU), Singapore, Singapore. [8] Hubei Key Laboratory for Heavy Rain Monitoring and Warning Research, Institute of Heavy Rain, China Meteorological Administration (CMA), Wuhan, China. [9] Key Laboratory of Transportation Meteorology of China Meteorological Administration (KLTM), Nanjing Joint Institute for Atmospheric Sciences, Nanjing, China. [10] Center of Water Management and Climate Change, Vietnam National University (VNU), Ho Chi Minh City, Vietnam. ✉e-mail: jingyu.wang@nie.edu.sg; zhi@nuist.edu.cn

In mid-April and early May 2023, a record-breaking heatwave affected many SEA countries, especially over the Continental Southeast Asia (CSEA; see box in Fig. 1a). 70% of all weather stations in Thailand, Laos, Cambodia, Myanmar's, and Vietnam have recorded daily maximum temperatures exceeding 42 °C (Fig. 1a). Notably, on 19 April, Laos's Sainyabuli province set a new all-time national highest temperature record of 42.9 °C[14]. Subsequently, from 1 May to 10 May (Fig. 1b), Thailand documented its highest temperature record reaching 49 °C[15] in Bangkok. Meanwhile, Vietnam also broke the country's previous record of 43.4 °C with a new maximum temperature of 44.1 °C[16,17]. Within the same time frame, on 7 May, Myanmar's Magway Region registered a peak temperature of 46 °C, leading to 61 heat-related fatalities[18] (the summary map is shown in Fig. S1). By taking the domain average daily temperature, the extreme happened in May 2023 stands unmatched in comparison to historical records dating back to 1950 (Fig. 1c).

Although the intensity of this heatwave event is unprecedented, its spatiotemporal distribution remains to be revealed, and the underlying physical processes are yet to be explored. These aspects will be systematically investigated for the first time in our study. Meanwhile, the forecast performance of this heatwave event will also be analyzed[19]. Finally, we will quantify the likelihood of future occurrence of such extreme event and its extensive impacts. Through this study, we aim to provide valuable insights into the nature and potential risks of extreme heatwaves over the region, empowering decision-makers to develop more effective risk management measures.

Results

Characteristics of the 2023 SEA heatwave

The spatiotemporal evolution of the heatwave event was examined over CSEA by analyzing the spatiotemporal evolution of areas with record-breaking temperatures at different timescales (see Methods) (Fig. 1d)[20,21]. Initially, the onset of record-breaking temperatures was observed from 14 to 22 April at the daily to 17 day timescale (Fig. 1d, e). During the first episode, the maximum daily temperature exceedance coverage was 266,000 km^2, accounting for 20% of the entire CSEA domain. However, the second episode of extreme temperatures that occurred on 4–7 May was more devastating. The impacted area extended over 560,000 km^2, covering 42% of the domain, causing severe local impacts over Myanmar, Laos, Thailand, Cambodia, and Vietnam and >60 deaths[14–17]. Following the peak, two subsequent episodes of high temperatures occurred from 18 to 22 May and from 28 May to 2 June, with elongated duration but diminishing spatial coverage (29% and 19% respectively). Upon examining the dates with highest temperatures (Fig. 1b), it becomes evident that the majority of the readings exceeding 42 °C were registered during the second episode of heat, marking this short-lived episode as the peak in terms of both severity and spatial coverage, which would be the focus of the following analyses.

Synoptic conditions

The analysis of synoptic conditions conducive to the peak heatwave episode were split into pre-event (28 April-1 May; Fig. 2a, d, g), peak (4-7 May; Fig. 2b, e, h), and post-event (9–12 May; Fig. 2c, f, i) periods. During the pre-event period, a widespread high-pressure anomaly at 925 hPa (Z925) dominated CSEA and South China (Fig. 2a). Additionally, there was a high-pressure anomaly over CSEA at 500 hPa (Z500), resulting in a configuration reminiscent of the conventional "heat dome" pattern as depicted in many studies of significant heatwave events[22–24], wherein an exceptionally high-pressure blocking system in the upper troposphere confine scorching air in the lower troposphere. Meanwhile, the low-level northeasterly wind brought dry-cold air and contributed to the negative moisture advection over CSEA (Fig. 2d and Fig. S2g). As a result, the negative anomaly in relative humidity (RH) of -5% at 925 hPa (RH925) and the limited cloud cover fraction (Fig. S3a, d) were observed, which allowed more incoming solar radiation and contributed to surface warming over CSEA.

During the peak episode, the Z500 high-pressure anomaly intensified over CSEA (Fig. 2b), which can be partly attributed to the southwestward expansion of the Western Pacific Subtropical High (WPSH; defined by the 5880 geopotential meter [gpm] contour; Fig. S4), leading to enhanced subsidence in the atmospheric column above this region (Fig. 2h). This situation contributed to the notable moisture divergence over CSEA (Fig. S2b, e) and exacerbated the negative moisture anomaly over CSEA. Meanwhile, a strong low-pressure system developed over South China (SC), which contributed to significant moisture convergence over SC and caused the severe rainstorm over Jiangxi Province (Fig. 2b and Fig. S5)[25]. This strong low-pressure system exacerbated the moisture divergence over CSEA by deflecting moisture that was supposed to be transported to the CSEA towards SC. As a result, a further decrease in RH of 7% over CSEA relative to the pre-event period (from 70% to 63%, Fig. 2d, e) was observed and the cloud coverage was reduced by ~30% compared to the pre-event period (Fig. S3b, e). Such reduction allowed more solar radiation to reach the ground, leading to rapid surface warming. On the other hand, after being heated during the pre-event period, the near-surface pressure anomaly also transitioned to negative state over CSEA (Fig. 2b). However, it is difficult for such a shallow low-pressure system to stimulate convection due to the lack of moisture supply and the strong downward motion from upper levels. This warm-core low structure has also been considered as the common setup for dry heatwaves over CSEA[26].

Regarding the post-event period, the high-pressure system over CSEA weakened significantly with the eastward retreat of WPSH (Fig. 2c and Fig. S4). Meanwhile, a low-level cyclonic circulation formed over the east coast of Vietnam (Fig. 2f), which contributed to the moisture convergence (Fig. S2f) and upward motion over CSEA (Fig. 2i). Besides, extreme tropical cyclonic storm Mocha emerged over the Bay of Bengal (Fig. 2c)[27], transporting moisture from the ocean to the CSEA and further exacerbated the moisture convergence there (Fig. S2f, j). The combination of these two low-pressure systems resulted in the positive RH anomalies and abundant cloud formation over CSEA (Fig. S3c, f), which led to a decrease in surface solar radiation and brought precipitation to the region, inducing cooling and ultimately marking the end of the extreme heatwave episode (Fig. S5).

Interaction of tropical waves

As mentioned above, the enhanced high-pressure system and the moisture deficiency over CSEA played important roles in the formation of this extreme heatwave event. Previous studies highlighted that the tropical weather systems are strongly modulated by the interplay of tropical waves[28–34]. To further analyze the driving forces of the synoptic conditions contributing to this peak heatwave episode, the roles of several tropical modes including Equatorial Rossby (ER) wave, Kelvin wave, Mixed-Rossby Gravity (MRG) wave, and Madden-Julian Oscillation (MJO) are explored. A wavenumber-frequency spectral analysis (see Methods) was conducted by decomposing these tropical waves' individual contribution to the CSEA regional outgoing longwave radiation (OLR, Fig. 3a).

During the peak episode (4–7 May), the regional average OLR over CSEA reached the maximum (Fig. 3a), indicating the most intense solar radiation and the absence of convective activity in the area, both facilitated the accumulation of heat. These days also corresponded to the highest regional average temperatures (red bars in Fig. 3a). ER and Kelvin waves were the primary contributors to the positive OLR anomalies during this period. This can be further confirmed by the Hovmöller diagram of OLR Anomalies (Fig. 3b), which shows that CSEA was influenced by the westward-propagating ER (red dashed line), the eastward-propagating Kelvin (green dashed line) waves. Notably, ER wave at peaking phase has been proven to enhance the middle and upper level convergence[32], thereby strengthening the westward-propagating Z500 high-pressure system mentioned above. As a result, the subsidence in the atmospheric column above CSEA was severely intensified (Fig. 2h).

Meanwhile, such east-west asymmetry between ER and Kelvin waves favored strengthening of MJO, known as the "acceleration effect"[35–38]. According to the phase diagram (Fig. 3c), MJO transitioned into Phase 4 on 30 April and rapidly advanced into Phase 5 from 6 to 7 May (Fig. 3d). The phase 4 is favorable for the westward expansion of WPSH and the

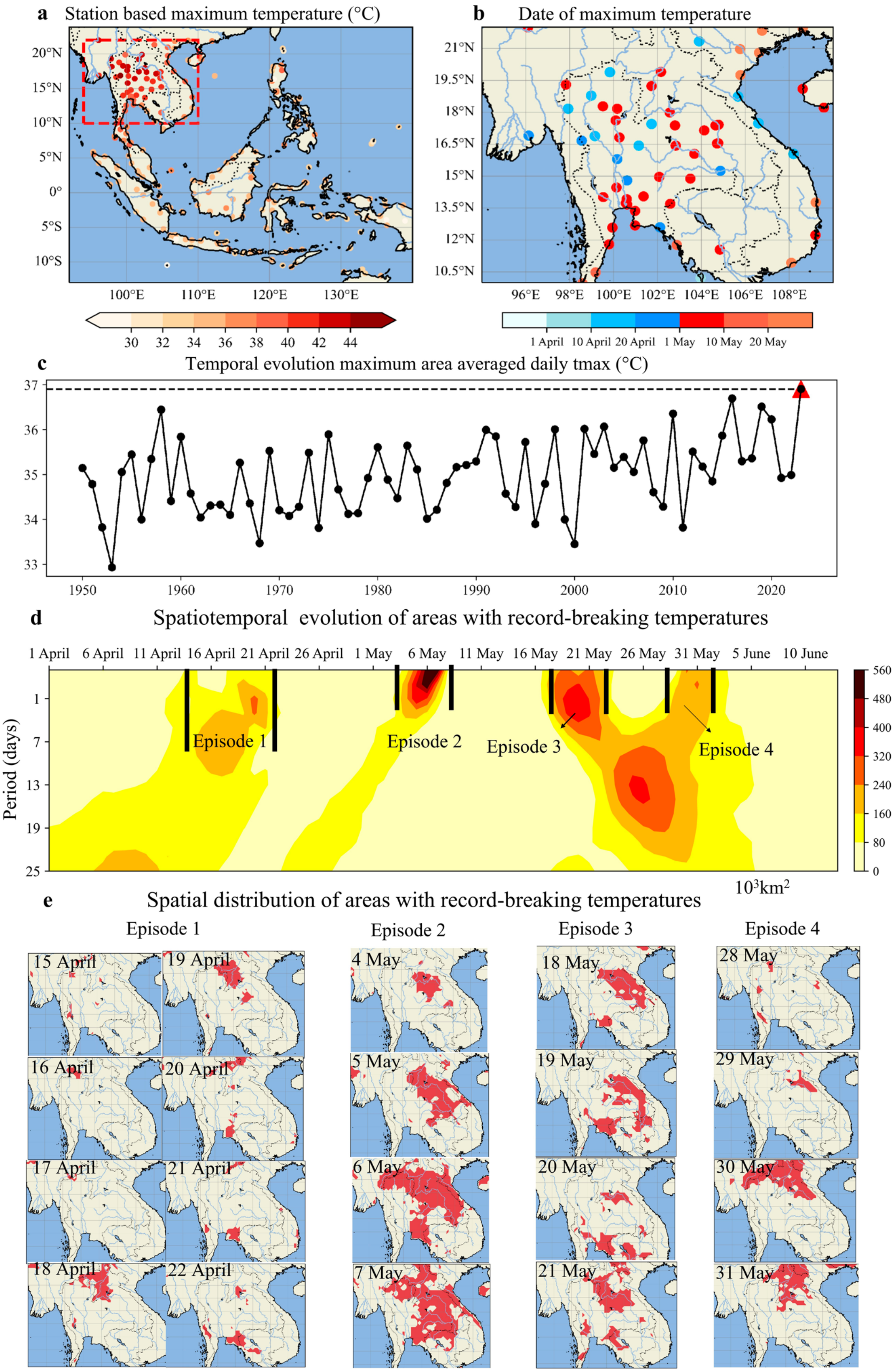

Fig. 1 | Characteristics of the 2023 CSEA heatwaves. **a** Daily maximum temperature from weather stations during April-May 2023. The red box is the region of Continental Southeast Asia (CSEA). **b** The date of the highest daily maximum temperature occurrence at each station in CSEA. **c** The temporal evolution of the average daily maximum temperature during April-May in CSEA. The red triangle indicates the peak regional average daily maximum temperature in 2023. **d** Spatiotemporal evolution of spatial extent (in $10^3\,km^2$) of areas with record-breaking temperatures at different timescales (from 1 to 31 days; see Methods). The black vertical lines in this figure mark the duration of each episode. **e** The spatial distribution of areas with record-breaking temperatures in each episode. Areas shaded in red indicate the occurrence of record-breaking temperature for each grid element on that day.

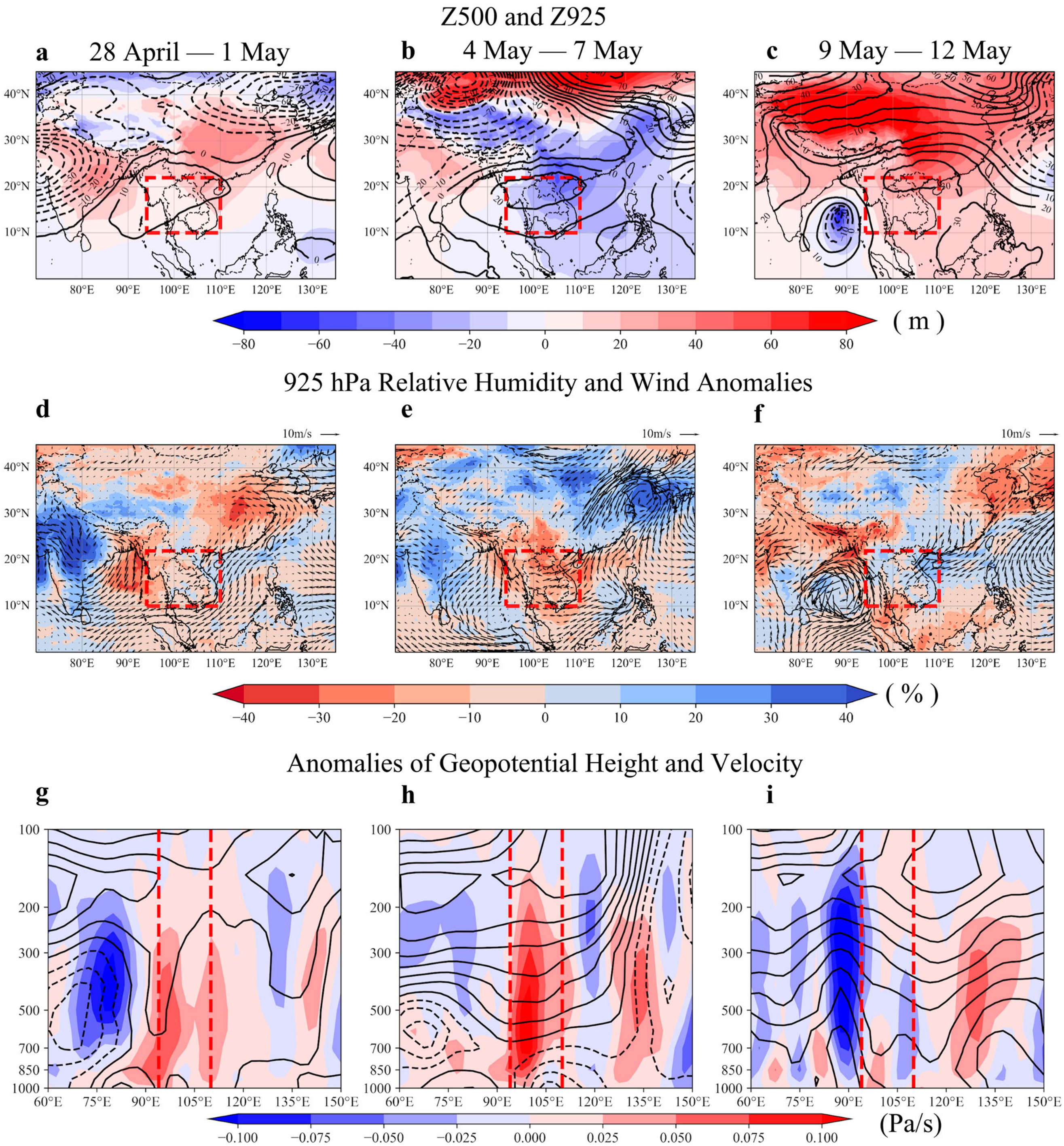

Fig. 2 | Meteorological conditions leading up to the heatwave. a–**c** The average 4 day Z500 (contour) and Z925 (shading) anomalies during 28 April-1 May (before the heatwave), 4–7 May (peak of the heatwave) and 9-12 May (after the heatwave). The red boxes represent the CSEA region with the solid and dashed lines indicating positive and negative anomalies, respectively. **d**–**f** Same as (**a**–**c**) but for 925 hPa relative humidity and wind Anomalies. **g**–**i** Same as (**a-c**) but for anomalies of pressure velocity (shading) and geopotential height (contour) along the longitude-height cross section averaged over the latitudes between 10 °N and 22 °N.

strengthening of the Z500 high-pressure system over CSEA (Fig. 3d). As documented in previous studies[39,40], when MJO turns into phase 5, WPSH typically expands eastward, facilitating convection at Bay of Bengal and South China Sea. It is noteworthy that MJO exhibited significant activity on 4-7 May with an amplitude peaking at 2.6, exceeding 95% of all historical records in Phase 4 as well as all records for Phase 4 in May (based on the records from 1974 to 2023). Thus, the MJO played an important role in modulating the high-pressure system over CSEA in the peak period of this extreme heatwave event.

Land-atmosphere coupling

In addition to atmospheric forcing mechanisms, the role of land-atmosphere coupling has also been highlighted as an important factor in extreme heatwaves[41,42]. High temperatures dry the soil by increasing evaporation and plant transpiration, while drier soil intensifies surface warming by reducing evaporative cooling and increasing upward sensible heat flux[43,44]. Meanwhile, soil moisture reduction favors a positive geopotential height anomaly in the upper levels, maintaining local high pressure and furtherly promoting surface warming[45]. Such positive land-atmosphere

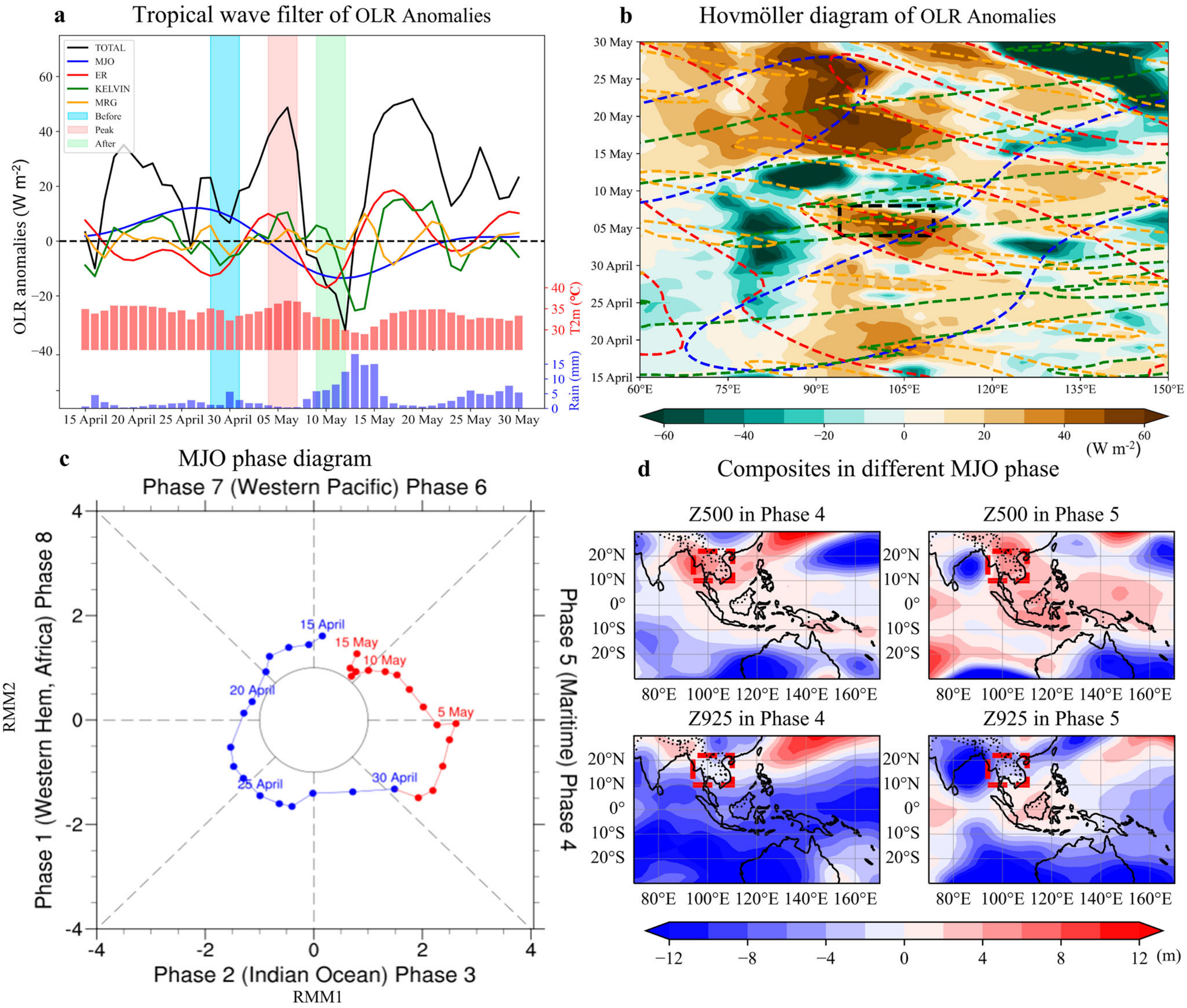

Fig. 3 | Tropical waves analysis and MJO states. a The temporal evolution of the average wavenumber-frequency-filtered OLR anomalies (see Methods) of tropical waves over the CSEA region, accompanied by the corresponding regional average daily maximum temperatures (red bar) and daily total precipitation (blue bar). **b** Date-longitude Hovmöller diagram of the OLR anomalies (shading) averaged between 10°N and 22°N. The contours indicate the filtered OLR anomalies of the tropical waves (only 4 wm^{-2} contours are shown): the Madden-Julian Oscillation (blue), Equatorial Rossby wave (red), Kelvin waves (green) and Mixed-Rossby Gravity (orange). The black box represents the CSEA during the peak of the heatwave. **c** The temporal evolution of MJO phase from 15 April to 5 May. The axes (RMM1 and RMM2) represent daily values of the Real-time Multivariate MJO Indices from the two leading modes, where dots denote the dates and distance from the origin is proportional to MJO strength. **d** The composites of 500 hPa geopotential height (Z500) and 925 hPa geopotential height (Z925) anomalies for May ranging from 1994 to 2023 in active MJO phase 4 and 5. The active MJO events are defined as the MJO amplitudes from the RMM index > 1. The red boxes represent the CSEA region.

feedback can increase the likelihood of extreme high temperatures and has been considered to play crucial roles in the development of heatwaves over northern Europe, North American, and even over moist eastern China[46–48]. Thus, it is important to investigate the role played by the land-atmosphere coupling in intensifying the magnitude of this extreme heatwave event.

The land-atmosphere coupling strength can be quantified by using π diagnostic of soil moisture–temperature coupling[49](see Methods). During the pre-event period, about half of the CSEA was characterized by negative soil moisture anomalies (Fig. 4a). This can be attributed to the "heat dome" pattern and the reduced cloud cover, which contributed to surface warming and increased soil moisture depletion. In this context, the land-atmosphere coupling was not evident and only occurred in some areas with severe soil moisture deficits (Fig. 4d). During the peak episode, the air became drier and hotter, which promoted stronger depletion of soil moisture, leading to substantial negative soil moisture anomalies across most of the CSEA (Fig. 4b). Corresponding, the land-atmosphere coupling strength intensified rapidly (Fig. 4e), which enhanced surface warming by increasing upward sensible heat flux. Specifically, the strong sensible heat (-70 W m^{-2}, 13% higher than pre-event) was emitted to the atmosphere during the peak period (Table S1). It is noteworthy that areas of strong land-air coupling strength are highly consistent with regions of extreme high temperatures during this heatwave episode (Fig. 4e and Fig. 1e), further highlighting the crucial role played by land-surface coupling in intensifying the magnitude of this extreme heatwave event. Regarding the post-event period, the soil moisture increased significantly due to the return of precipitation, leading to positive soil moisture anomalies across most of the CSEA region and contributing to a rapid decrease in land-atmosphere coupling strength (Fig. 4c, f).

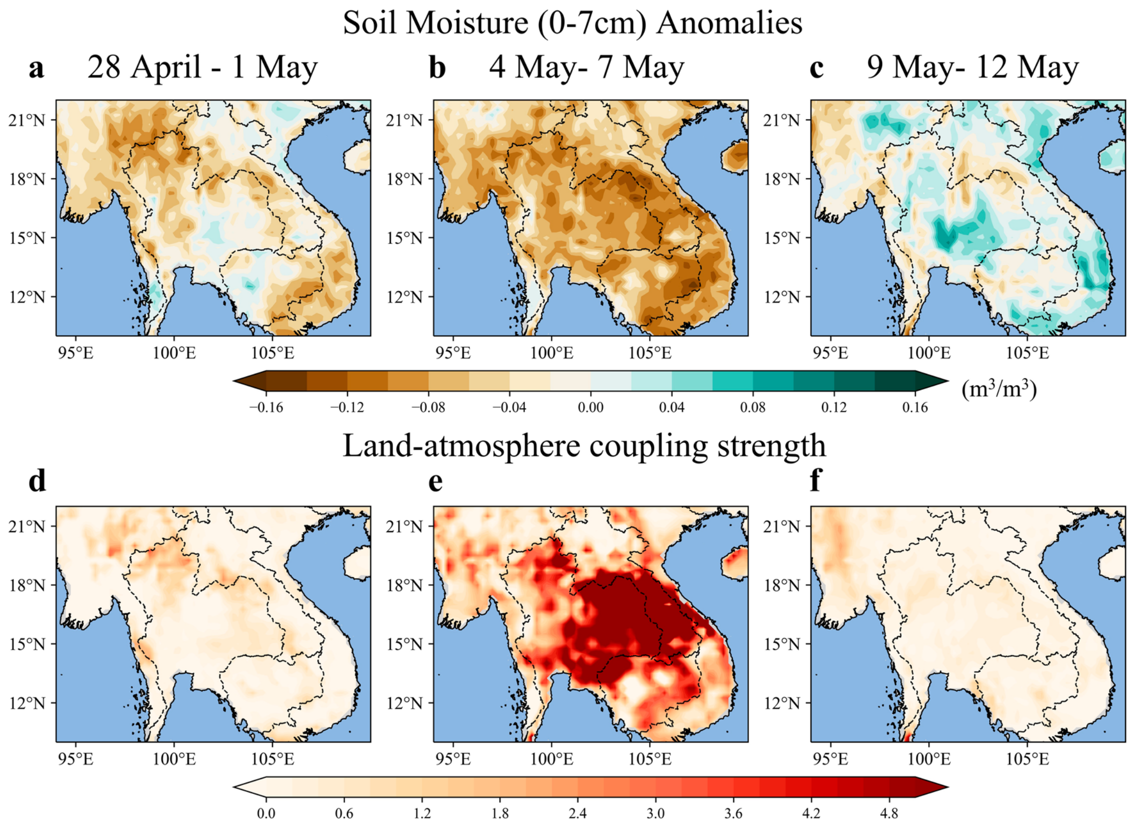

Fig. 4 | Land-atmosphere coupling. **a**–**c** The average 4 day soil moisture (0–7 cm) anomalies during 28 April-1 May (before the heatwave), 4–7 May (peak of the heatwave) and 9–12 May (after the heatwave). **d**–**f** Same as (**a**–**c**) but for land-atmosphere coupling strength.

Forecasts

The ability to forecast extreme events at longer lead times can significantly enhance early warning and strengthen mitigation efforts preparation systems. In this study, we analyzed the prediction of this heatwave event using the European Centre for Medium-Range Weather Forecasts (ECMWF) operational S2S forecasts[50–55]. Figure 5 indicates the ECMWF forecasted spatial distribution of the ongoing heatwave process effectively at 1 week lead time (initialized on 1 May, Fig. 5b), but the intensity was underestimated by 1 °C. Furthermore, the forecast skill of ECMWF for this heatwave event decreased rapidly with the increasing lead times. Specifically, the ECMWF predicted the maximum positive temperature anomaly center near Laos and Thailand but overlooked high temperatures in other areas (Fig. 5c–f). Meanwhile, the forecasted intensity of positive temperature anomalies was significantly lower than the observed values.

To explore the reasons behind ECMWF's diminished forecasting accuracy for this heatwave event, we examined the forecasts of the enhanced high-pressure, the decreased relative humidity and the land-atmosphere coupling, which are considered as the key factors conducive to the extreme heatwave episode. The results show that the ECMWF demonstrated high forecast skills for the enhanced high-pressure system and negative relative humidity anomalies (Fig. S6), but exhibited limited skills for the soil moisture anomalies even at 1 week lead time (Fig. 5h). This indicates that ECMWF struggles to capture the strong land-atmosphere coupling during this extreme heatwave event, leading to a cold bias and contributing to the underestimation of heatwave intensity[56]. Furthermore, while the forecast skills for atmospheric conditions declined rapidly with increasing lead times—evidenced by rising mean absolute errors (MAEs) and decreasing pattern correlation coefficients (PCCs; Fig. S6 and Table S2)—the skill for soil moisture prediction remained consistently low across all lead times. This suggests that ECMWF's deficiency in simulating soil moisture may introduce systematic cold biases, while the decreasing forecast skill for atmospheric conditions likely contributed to the rapid deterioration of heatwave forecast skills.

Return period

Analyzing the probability of extreme event occurrences can assist decision-makers in better understanding the potential risks of future extremes, enabling the implementation of more effective risk management measures. In this study, the return period of this heatwave episode is calculated based on the statistical distribution for extreme events using the generalized extreme value (GEV) distribution and maximum likelihood estimates[57]. Result indicated that the return period of this event with 4 day mean temperature exceeding 34.3°C (averaged over the CSEA) was 129 years (Fig. 6a). Following previous studies[58,59], the joint probability density of key drivers to the extreme events are also calculated to provide a robust estimation of their return period. As discussed in previous sections, the enhanced high-pressure, the reduced moisture and the land-atmosphere coupling served as the key factors in this heatwave event. Thus, the 4 day mean Z500, RH925 and soil moisture (SM) anomalies during April to May ranging from 1950 – 2023 are analyzed in Fig. 6b-d.

As depicted in Fig. 6b, the joint probability for high value in Z500 anomalies and low value in RH925 anomalies (quadrant 4) in this event was 0.15%. This indicates that the combination of such enhanced high-pressure system and near-surface dryness is an uncommon setup over CSEA. Moreover, the joint probability for Z500 and SM anomalies in this event was 0.30%, while the joint probability for RH925 and SM anomalies was exceptionally rare at 0.08%. As a result, the simultaneous occurrence of the three pivotal factors leading to this extreme heatwave episode was absolutely unprecedented, particularly the synergistic impact of near-surface drying and soil moisture deficiency, which could stimulate strong positive land-atmosphere feedback and leading to rapid warming.

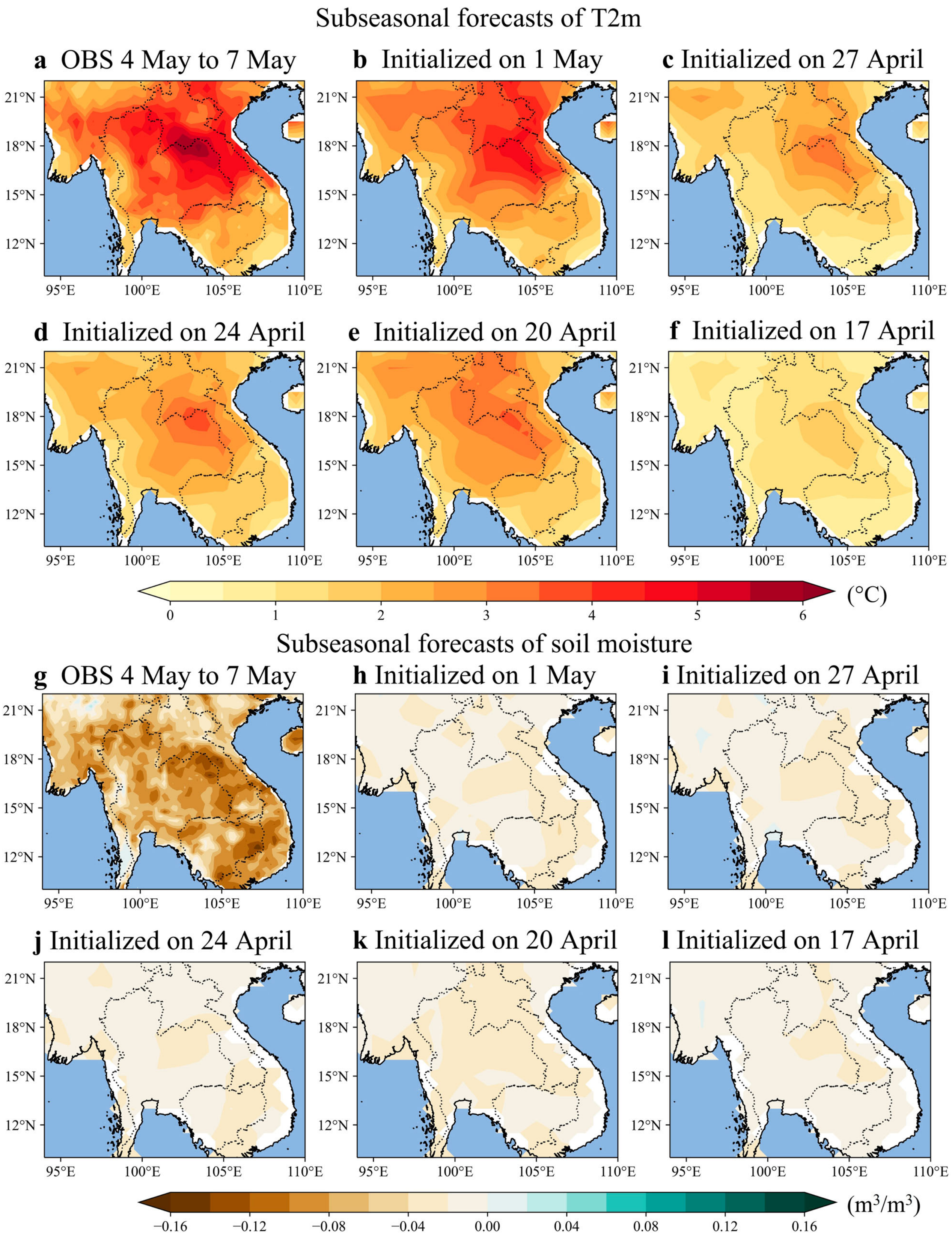

Fig. 5 | Subseasonal forecasts of the temperature and soil moisture. a The observed daily mean 2 m temperature (T2m) anomalies averaged from 4 May to 7 May (the peak of this heatwave) over CSEA. The corresponding forecasts from ECMWF initialized on 1 May (**b**), 27 April (**c**), 24 April (**d**), 20 April (**e**), and 17 April (**f**). **g–l** same as (**a–f**) but for soil moisture anomalies.

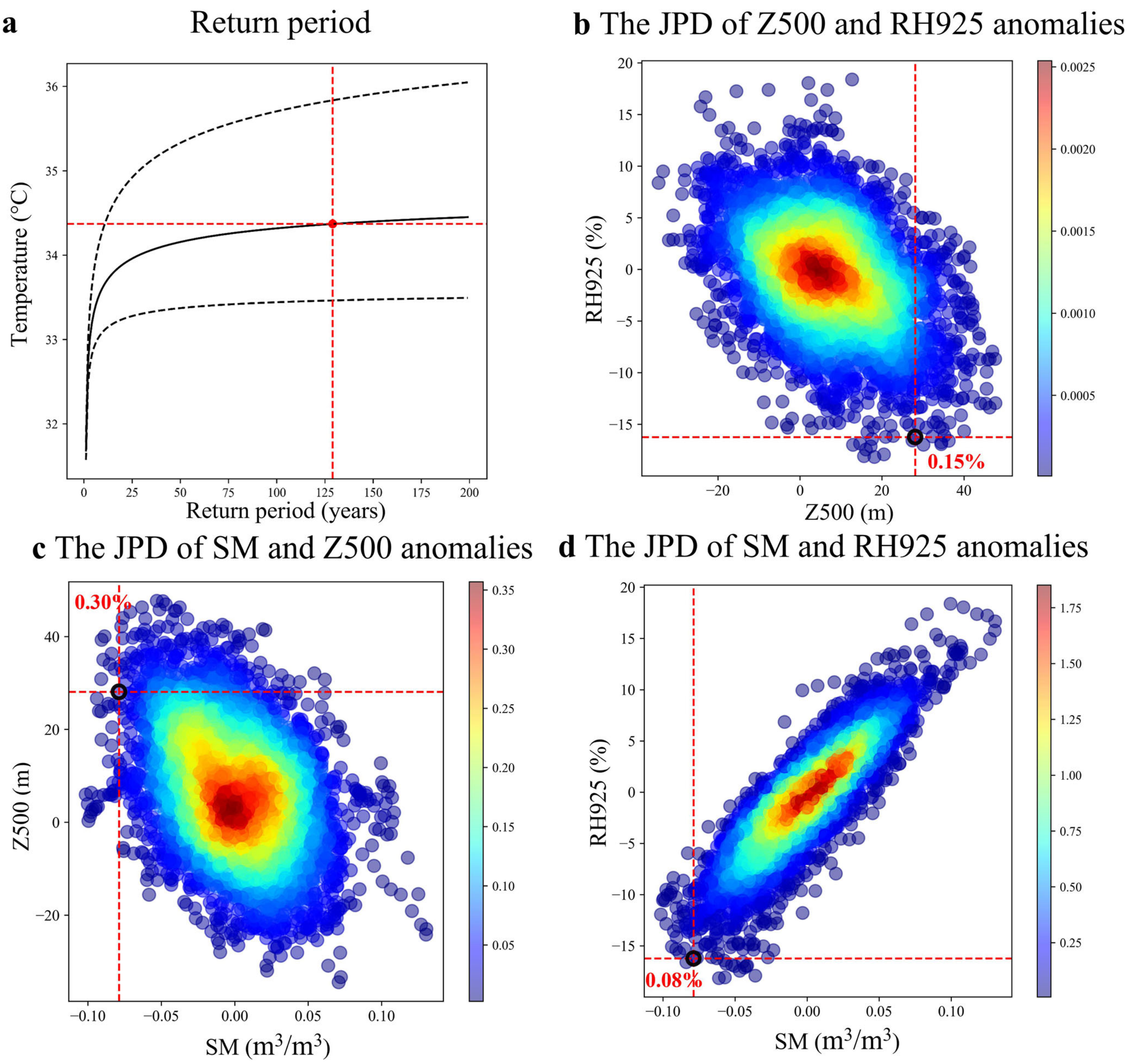

Fig. 6 | Return period analysis of the heatwave. a The return period of the heatwave calculated from generalized extreme value (GEV) distribution and maximum likelihood estimates (see Methods). The red dot is the average 4 day mean daily maximum temperature over CSEA in the peak of this heatwave (4–7 May). **b** The joint probability density (JPD) for 500 hPa geopotential height (Z500) and 925 hPa relative humidity (RH925) anomalies. The black dot is the observed Z500 and RH925 in this event. **c** Same as (**b**) but for soil moisture (SM) and Z500 anomalies. **d** Same as (**b**) but for SM and RH925 anomalies. The associated joint probabilities for these factors are also provided.

Impacts

The prolonged and arid weather conditions accompanying the heatwave desiccated the vegetation over the region, leading to heightened fire risk and a surge in wildfire incidents. Figure S7a, b depicts the spatial distributions of monitored fire spots over the CSEA region on 4 May, as observed by the Moderate Resolution Imaging Spectroradiometer (MODIS) aboard Terra and Aqua satellites. Through the quantification of fire spots with 4-day interval in May since 2003 (Fig. S7c, d), the studied 2023 peak heatwave episode featured an unparalleled number of fire spots at both medium and high confidence observed by Terra.

In addition to the surge in wildfires, heatwaves have the potential to significantly reduce annual yields as temperatures surpass crop-specific thresholds, leading to substantial declines in production[60]. Rice is one of the most crucial staple crops in SEA, and it exhibits high sensitivity to elevated temperatures, particularly during the germination and flowering stages[61–64]. In addition to the diminished quality and reduced yield caused by elevated temperature stress, hot weather conditions also exert an impact on the labor involved in the planting and harvesting process[65,66]. Fig. S8 illustrates the rice production and respective growing seasons for Myanmar, Laos, Thailand, and Cambodia since 2013. With advancements in cultivation techniques and the introduction of more resilient and productive varieties, Laos, Thailand, and Cambodia have shown an increasing trend in annual rice production, while Myanmar has experienced a persistent decline probably due to an unstable political situation. However, the annual rice production of each country has been evidently influenced by the studied heatwave events in 2023, attributing to the fact that May marks the beginning of planting and the middle of harvesting seasons.

Discussion

This study delivers a comprehensive examination of the "once-in-200 year" Southeast Asia heatwave event in April-May 2023 with the focus of the unprecedented extreme heatwave episode on 4–7 May, covering its spatiotemporal evolution, physical mechanism, forecast performance, return period, and extensive impacts. The 2023 heatwave event has brought far-reaching consequences over CSEA, with all countries experiencing record-breaking temperatures. The regional average daily maximum temperature also reached its highest level since 1950, severely affecting people's lives and properties, leading to unparalleled wildfires, and causing a substantial reduction in rice yields.

Synoptic analysis indicated that the enhanced local high-pressure system affected by the tropical waves played a dominant role in the formation of this extreme heatwave event, which brought strong subsidence in the atmospheric column above this region and contributed to the notable moisture divergence over CSEA. Meanwhile, the strong moisture convergency over SC also exacerbated the moisture divergence over CSEA. As a result, the cloud cover over CSEA was severely reduced, causing more solar radiation and resulting in rapid warming. The temperature budget at Z925 analysis indicated that the diabatic heating played the most important role in heatwave formation (Text S1 and Fig. S9). Besides, the persistent warming over CSEA region intensified soil moisture depletion, which in turn contributed to further warming by reducing evaporative cooling and increasing upward sensible heat flux during the peak episode of this heatwave event (Fig. S9 and Table. S1). Consequently, the positive feedback mechanism of land-atmosphere coupling also played a crucial role in exacerbating the severity of this extreme heatwave event.

In terms of predictability, the European Centre for Medium-Range Weather Forecasts (ECMWF) successfully forecasted the spatial pattern of the extreme heatwave at 1 week lead time, though the intensity was underestimated by 1 °C and its forecast skill decreased rapidly with increasing lead times. Further analysis revealed a systematic deficiency in simulating soil moisture across all lead times, which may introduce persistent cold biases that compound the rising atmospheric errors, ultimately reducing the accuracy of heatwave forecasts with increasing lead times.

To assess the future probability of such extreme event, both return period calculation and joint probability analysis of the key drivers were conducted. The results indicated that the return period for this event, characterized by a 4 day mean temperature exceeding 34.3 °C (averaged over the CSEA), was 129 years. Furthermore, the combination of near-surface drying and soil moisture deficiency, which could trigger strong positive land-atmosphere feedback and lead to rapid warming, was exceptionally rare, with an occurrence probability of just 0.08%. These analyses underscore the extremity of this heatwave event and the crucial role of land-atmosphere coupling in exacerbating the heatwave severity.

This unprecedented heatwave event showed significant impacts on lives, ecosystems, and agriculture. As one of the most important agricultural heartlands with a dense population, accurate heatwave prediction in CSEA is urgent for ensuring food security and safeguarding public health at both local and regional scales. Therefore, further research should be focused on exploring advanced forecast skills, such as deepening the understanding of key drivers and their representation in dynamical models[67], establishing statistical model based on physical progress analysis[68,69], and integrating dynamical models with machine-learning techniques[70,71].

Methods

Overview/Introduction

To analyze heatwave temperature, the gridded daily maximum 2 m temperature data ranging from 1950 – 2023 from ERA5 reanalysis[72], along with the station data for 2023 from Global Historical Climatology Network daily (GHCNd)[73] were utilized. The GHCNd dataset contains meteorological measurements from over 90,000 stations across the globe and was utilized for the validation of temperature estimates from satellites and atmospheric reanalysis.

Table 1 | The characteristics of each tropical mode

Mode	Wavenumber band	Period band (days)	Equivalent depth (m)
MJO	0–9	20–100	Not specified
ER	10 to -1	9.7–72	1–90
KELVIN	1 to 14	2.5–20	8–90
MRG	−10 to −1	3–96	8–90

To characterize the magnitude and spatiotemporal evolution of this event, we identified areas with record-breaking temperatures at different timescales over target region (denoted as dashed red boxes in the Fig. 1a) for April-June 2023. Following previous studies[20,21], We calculated the moving average of daily maximum 2 m temperature with windows from 1 to 29 d for each April–June day from 1950–2023. For each calendar day and time scale in April-June 2023, one grid with the highest temperature during the period 1950–2023 was identified as the record-breaking grid. We then calculated the area of record-breaking temperature for each day and timescale in April-June 2023 (Fig. 1c). The spatial patterns of record-breaking temperatures are also shown in Fig. 1d.

Synoptic conditions and the interaction of tropical waves

The daily mean ERA5 reanalysis data for geopotential height, zonal wind component, meridional wind component, vertical wind component, specific humidity and relative humidity at various pressure levels in the atmosphere are utilized. Daily anomalies were calculated relative to the 1981–2010 mean of each calendar day. The outgoing long-wave radiation (OLR) from ERA5 is also utilized to conduct tropical wave analysis. The details are as follows:

Firstly, the mean and first three harmonics of the OLR annual cycle are removed to obtain intraseasonal anomalies. Then, a wavenumber–frequency spectral analysis was executed for all latitudes within the meridional band of 25°S–25°N based on the NCAR command language (NCL) script filter_waves, available from Dr. C. Schreck at GitLab (https://k3.cicsnc.org/carl/carl-ncl-tools/blob/master/filter/filter_waves.ncl). In this study, the contribution of four tropical waves including MJO, ER, KELVIN and MRG to intraseasonal anomalies are analyzed. The characteristics of each mode are defined as previous studies[74–77] and can be found in Table 1.

Land-atmosphere coupling

The strength of land-atmosphere coupling can be quantified by using π diagnostic of soil moisture–temperature coupling, which is based on two energy balances of evaporation and potential evaporation. This metric has been widely utilized in previous heatwave studies[42,46,78]. Based on the daily, the strength of land-atmosphere coupling can be defined as:

$$\pi = e' \times T' \tag{1}$$

$$e' = H' - H_p' = \left(R_n - \lambda E\right)' - \left(R_n - \lambda E_p\right)' \tag{2}$$

where primes represent daily anomalies of each variable expressed as the number of standard deviations relative to the climatological mean. R_n refers to the surface net radiation, T is the daily temperature, E and E_p denote the actual and potential evaporation, respectively, and λ is the latent heat of vaporization. Following previous studies, the surface net radiation was calculated by subtracting the surface net thermal radiation from the surface net solar radiation[46,79]. The T, E, E_p, and R_n can be obtained from ERA5 reanalysis dataset. The e' is represented by $H' - H_p'$ and denotes the contribution of soil moisture deficiency to sensible heat flux. The energy term e' will be zero when the soil moisture is sufficient for the atmospheric demand, and it may increase under dry conditions. Positive values of π mean the stronger soil moisture–temperature coupling. The local energy balance solely controls the atmospheric temperature if the potential effect of soil moisture on temperature is accompanied by large anomalous temperature values.

Subseasonal forecast

For the subseasonal forecast, we use the state-of-the-art ECMWF Integrated Forecasting System (IFS) model, one of 11 models available as part of the S2S prediction project database[54]. The IFS has 51 forecast ensemble members, with 11 reforecast members implemented over the previous 20 years, and a maximum resolution of 0.5°. Forecasts and reforecasts are initialized twice a week. Previous studies consistently highlight ECMWF as a leading subseasonal dynamical model, demonstrating superior forecasting skills over other models[80–82]. Specifically, the good performances of ECMWF are demonstrated up to lead times of 7–10 days for extreme cold events, up to 15 days for heatwaves over some certain regions[83–85].

Considering the observed synoptic conditions, the forecasts of 2 m temperature (T2m), geopolitical heights at 500hpa (Z500), relative humidity at 925hpa (RH925) and soil moisture (SM; 0-7 cm) anomalies are analyzed, which are calculated by subtracting the 20 year average from the respective reforecasts. The soil moisture in the 0-7 cm layer is obtained by interpolating the soil moisture from the 0-20 cm layer based on distance. We mainly focus on the 4 day average conditions during the peak time of this event (from 4 to 7 May) and five initialized time are considered: 1 May, 27 April, 24 April, 20 April, and 17 April, which correspond to the lead time of 3–6, 7–10, 10–13, 14–17 and 17–20 days.

Data availability

The ERA5 reanalysis data can be obtained from https://cds.climate.copernicus.eu/cdsapp#!/home. The subseasonal forecast data from ECMWF can be downloaded at https://apps.ecmwf.int/datasets/data/s2s/. The agricultural yield data were obtained from the United States Department of Agriculture (USDA) Foreign Agricultural Service (https://ipad.fas.usda.gov/countrysummary/Default.aspx?id=TH&crop=Rice). The MODIS fire spot data were downloaded from NASA's Land Processes Distributed Active Archive Center (LP DAAC) located at the USGS Earth Resources Observation and Science (EROS) Center. The Terra data are available at https://e4ftl01.cr.usgs.gov/MOLA/MOD14A1.061/, and the Aqua data are available at https://e4ftl01.cr.usgs.gov/MOLT/MYD14A1.061/. The daily averaged cloud fraction data were downloaded from Level-1 and Atmosphere Archive & Distribution System Distributed Active Archive Center (LAADS-DAAC). The Terra data are available at https://ladsweb.modaps.eosdis.nasa.gov/archive/allData/61/MOD08_D3. The Aqua data are available at https://ladsweb.modaps.eosdis.nasa.gov/archive/allData/61/MYD08_D3.

Received: 12 April 2024; Accepted: 4 October 2024;
Published online: 14 October 2024

References

1. Perkins-Kirkpatrick, S. E. & Lewis, S. C. Increasing trends in regional heatwaves. *Nat. Commun.* **11**, 3357 (2020).
2. Robine, J. M. et al. Death toll exceeded 70,000 in Europe during the summer of 2003. *Comptes Rendus. Biologies* **331**, 171–178 (2008).
3. Rousi, E., Kornhuber, K., Beobide-Arsuaga, G., Luo, F. & Coumou, D. Accelerated western European heatwave trends linked to more-persistent double jets over Eurasia. *Nat. Commun.* **13**, 3851 (2022).
4. White, R. H. et al. The unprecedented Pacific Northwest heatwave of June 2021. *Nat. Commun.* **14**, 727 (2023).
5. Shaposhnikov, D. et al. Mortality related to air pollution with the Moscow heat wave and wildfire of 2010. *Epidemiology* **25**, 359–364 (2014).
6. Wuebbles, D. J. et al. Executive summary. In *Climate Science Special Report: Fourth National Climate Assessment* (eds. Wuebbles, D. J., et al.) 12–34 (Global Change Research Program, 2017)
7. Houze, R. A. Jr, Wang, J., Fan, J., Brodzik, S. & Feng, Z. Extreme convective storms over high-latitude continental areas where maximum warming is occurring. *Geophys. Res. Lett.* **46**, 4059–4065 (2019).
8. Sun, X., Ge, F., Chen, Q., Fraedrich, K. & Li, X. How striking is the intergenerational difference in exposure to compound heatwaves over southeast Asia? *Earth Future* **11**, e2022EF003179 (2023).
9. Ge, F., Zhu, S., Luo, H., Zhi, X. & Wang, H. Future changes in precipitation extremes over Southeast Asia: insights from CMIP6 multi-model ensemble. *Environ. Res. Lett.* **16**, 024013 (2021).
10. Fan, Y., Li, J., Zhu, S., Li, H. & Zhou, B. Trends and variabilities of precipitation and temperature extremes over Southeast Asia during 1981–2017. *Meteorol. Atmos. Phys.* **134**, 78 (2022).
11. Sun, X., Ge, F., Fan, Y., Zhu, S. & Chen, Q. Will population exposure to heat extremes intensify over Southeast Asia in a warmer world? *Environ. Res. Lett.* **17**, 044006 (2022).
12. Zhu, S. et al. Conspicuous temperature extremes over Southeast Asia: seasonal variations under 1.5 C and 2 C global warming. *Clim. Change* **160**, 343–360 (2020).
13. Li, X. X. Heat wave trends in Southeast Asia during 1979–2018: the impact of humidity. *Sci. Environ.* **721**, 137664 (2020).
14. Mishra, S. *One in Three People on the Planet Hit By 'Monster Asian Heatwave'.* https://doi.org/10.1200/JCO.2023.41.16_suppl.e13086 (2023).
15. Subramaniam, T. *Vietnam and Laos Record Hottest Temperatures Ever as Heat Wave Grips Southeast Asia.* https://www.cnn.com (2023).
16. *Temperature Records Shattered Across Asia as Heatwaves Continue.* https://www.worldweatherattribution.org (2023).
17. The Guardian. *Vietnam Records Highest Ever Temperature of 44.1C*. https://www.theguardian.com (2023).
18. Bhandari, S. R. *Heat Wave Blasts Southeast Asia—A Likely Pattern for the Future.* https://www.rfa.org/english/news/environment/heat-wave-05102023134526.html (2023).
19. Lin, H., Mo, R. & Vitart, F. The 2021 Western North American heatwave and its subseasonal predictions. *Geophys. Res. Lett.* **49**, e2021GL097036 (2022).
20. Barriopedro, D., Fischer, E. M., Luterbacher, J., Trigo, R. M. & García-Herrera, R. The hot summer of 2010: redrawing the temperature record map of Europe. *Science* **332**, 220–224 (2011).
21. Ren, L., Zhou, T. & Zhang, W. Attribution of the record-breaking heat event over Northeast Asia in summer 2018: the role of circulation. *Environ. Res. Lett.* **15**, 054018 (2020).
22. Reyes, L. & Kramer, M. G. High-elevation snowpack loss during the 2021 Pacific Northwest heat dome amplified by successive spring heatwaves. *npj Clim. Atmos. Sci.* **6**, 208 (2023).
23. Wang, W., Zhou, W., Li, X., Wang, X. & Wang, D. Synoptic-scale characteristics and atmospheric controls of summer heat waves in China. *Clim. Dyn.* **46**, 2923–2941 (2016).
24. Zhang, X. et al. Increased impact of heat domes on 2021-like heat extremes in North America under global warming. *Nat. Commun.* **14**, 1690 (2023).
25. Beiqing Net. *Heavy Rainfall in Jiangxi Affects 536,000 People and Causes 670 Million Yuan in Direct Economic Losses.* https://baijiahao.baidu.com/s?id=1765327590562294118&wfr=spider&for=pc&searchword=%E6%B1%9F%E8%A5%BF%E5%A4%9A%E5%9C%B0%E9%81%AD%E6%9A%B4%E9%9B%A8%E8%A2%AD%E5%87%BB (2024).
26. Luo, M. & Lau, N. C. Synoptic characteristics, atmospheric controls, and long-term changes of heat waves over the Indochina Peninsula. *Clim. Dynam.* **51**, 2707–2723 (2018).
27. Wikipedia. *Cyclone Mocha.* https://en.wikipedia.org/wiki/Cyclone_Mocha#:~:text=Extremely%20Severe%20Cyclonic%20Storm%20Mocha,of%20Bangladesh%20in%20May%202023 (2023).
28. Latos, B. et al. Equatorial waves triggering extreme rainfall and floods in southwest Sulawesi, Indonesia. *Monthly Weather Rev.* **149**, 1381–1401 (2021).

29. Guigma, K. H., Guichard, F., Todd, M., Peyrille, P. & Wang, Y. Atmospheric tropical modes are important drivers of Sahelian springtime heatwaves. *Clim. Dynam.* **56**, 1967–1987 (2021).
30. Zore, T., Landu, K., Gogoi, P. P. & Vinoj, V. Effect of tropical subseasonal variability on heatwaves over India. *Int. J. Climatol.* **41**, E2258–E2268 (2021).
31. Xavier, P., Rahmat, R., Cheong, W. K. & Wallace, E. Influence of Madden-Julian oscillation on Southeast Asia rainfall extremes: observations and predictability. *Geophys. Res. Lett.* **41**, 4406–4412 (2014).
32. Peyrillé, P., Roehrig, R. & Sanogo, S. Tropical waves are key drivers of extreme precipitation events in the Central Sahel. *Geophys. Res. Lett.* **50**, e2023GL103715 (2023).
33. Schumacher, C. & Houze, R. A. Jr Stratiform precipitation production over sub-Saharan Africa and the tropical East Atlantic as observed by TRMM. *Q. J. R. Meteorol. Soc.* **132**, 2235–2255 (2006).
34. Feng, Z. et al. A global high-resolution mesoscale convective system database using satellite-derived cloud tops, surface precipitation, and tracking. *J. Geophys. Res. Atmos.* **126**, e2020JD034202 (2021).
35. Nakamura, Y. & Takayabu, Y. N. Convective couplings with equatorial Rossby waves and equatorial Kelvin waves. Part I: coupled wave structures. *J. Atmos. Sci.* **79**, 247–262 (2022).
36. Wang, L., Li, T. & Nasuno, T. Impact of Rossby and Kelvin wave components on MJO eastward propagation. *J. Clim.* **31**, 6913–6931 (2018).
37. Sobel, A., Wang, S. & Kim, D. Moist static energy budget of the MJO during DYNAMO. *J. Atmos. Sci.* **71**, 4276–4291 (2014).
38. Wang, L., Li, T., Maloney, E. & Wang, B. Fundamental causes of propagating and nonpropagating MJOs in MJOTF/GASS models. *J. Clim.* **30**, 3743–3769 (2017).
39. Zhang, L., Wang, B. & Zeng, Q. Impact of the Madden–Julian oscillation on summer rainfall in southeast China. *J. Clim.* **22**, 201–216 (2009).
40. Wie, J., Kang, J. & Moon, B. K. Role of Madden–Julian oscillation in predicting the 2020 East Asian summer precipitation in subseasonal-to-seasonal models[J]. *Sci. Rep.* **14**, 865 (2024).
41. Miralles, D. G., Teuling, A. J., Van Heerwaarden, C. C. & Vilà-Guerau de Arellano, J. Mega-heatwave temperatures due to combined soil desiccation and atmospheric heat accumulation. *Nat. Geosci.* **7**, 345–349 (2014).
42. Zhang, P. et al. Abrupt shift to hotter and drier climate over inner East Asia beyond the tipping point. *Science* **370**, 1095–1099 (2020).
43. Jiang, J., Liu, Y., Mao, J. & Wu, G. Extreme heatwave over Eastern China in summer 2022: the role of three oceans and local soil moisture feedback. *Environ. Res. Lett.* **18**, 044025 (2023).
44. Dong, J. et al. Can surface soil moisture information identify evapotranspiration regime transitions?[J]. *Geophys. Res. Lett.* **49**, e2021GL097697 (2022).
45. Fischer, E. M., Seneviratne, S. I., Vidale, P. L., Lüthi, D. & Schär, C. Soil moisture–atmosphere interactions during the 2003 European summer heat wave. *J. Clim.* **20**, 5081–5099 (2007).
46. Ni, Y. et al. Shift of soil moisture-temperature coupling exacerbated 2022 compound hot-dry event in eastern China. *Environ. Res. Lett.* **19**, 014059 (2024).
47. Dirmeyer, P. A., Balsamo, G., Blyth, E. M., Morrison, R. & Cooper, H. M. Land-atmosphere interactions exacerbated the drought and heatwave over northern Europe during summer 2018. *AGU Adv.* **2**, e2020AV000283 (2021).
48. Bartusek, S., Kornhuber, K. & Ting, M. 2021 North American heatwave amplified by climate change-driven nonlinear interactions. *Nat. Clim. Change* **12**, 1143–1150 (2022).
49. Miralles, D. G., Van Den Berg, M. J., Teuling, A. J. & De Jeu, R. A. M. Soil moisture-temperature coupling: a multiscale observational analysis. *Geophys. Res. Lett.* https://doi.org/10.1029/2012GL053703 (2012).
50. Feng, J., Zhang, J., Toth, Z., Peña, M. & Ravela, S. A new measure of ensemble central tendency. *Weather Forecast.* **35**, 879–889 (2020).
51. Wang, S., Ma, D., Sobel, A. H. & Tippett, M. K. Propagation characteristics of BSISO indices. *Geophys. Res. Lett.* **45**, 9934–9943 (2018).
52. Kolstad, E. W., Macleod, D. & Demissie, T. D. Drivers of subseasonal forecast errors of the East African short rains. *Geophys. Res. Lett.* **48**, e2021GL093292 (2021).
53. Pegion, K. et al. The subseasonal experiment (SubX): a multimodel subseasonal prediction experiment. *Bull. Am. Meteorol. Soc.* **100**, 2043–2060 (2019).
54. Vitart, F. et al. The subseasonal to seasonal (S2S) prediction project database. *Bull. Am. Meteorol. Soc.* **98**, 163–173 (2017).
55. Vitart, F., Robertson, A. W. & Anderson, D. L. Subseasonal to seasonal prediction project: bridging the gap between weather and climate. *Bull. World Meteorol. Org.* **61**, 23 (2012).
56. Yoon, D. et al. Role of land–atmosphere interaction in the 2016 Northeast Asia heat wave: impact of soil moisture initialization. *J. Geophys. Res. Atmos.* **128**, e2022JD037718 (2023).
57. Jenkinson, A. F. The frequency distribution of the annual maximum (or minimum) values of meteorological elements. *Q. J. R. Meteorol. Soc.* **81**, 158–171 (1955).
58. Chang, C. P., Liu, C. H., & Kuo, H. C. Typhoon Vamei: an equatorial tropical cyclone formation. *Geophys. Res. Lett.* https://doi.org/10.1029/2002GL016365 (2003).
59. Dong, L. et al. Revealing the key drivers conducive to the “once-in-a-century” 2021 peninsular Malaysia flood. *Geophys. Res. Lett.* **50**, e2023GL106112 (2023).
60. Lesk, C., Rowhani, P. & Ramankutty, N. Influence of extreme weather disasters on global crop production. *Nature* **529**, 84–87 (2016).
61. Fuller D. Q., Castillo C. C. Cereals of southeast Asia[M]. In. *The Oxford Handbook of Early Southeast Asia, Oxford Handbooks* (eds. Charles F. W. Higham & Kim, N. C.) 299–320 (New York: Oxford University Press, 2022).
62. Xu, Y., Chu, C. & Yao, S. The impact of high-temperature stress on rice: challenges and solutions. *Crop J.* **9**, 963–976 (2021).
63. Ye, C., Li, X., Redoña, E., Ishimaru, T., & Jagadish, K. Genetics and breeding of heat tolerance in rice. In *Rice Improvement: Physiological, Molecular Breeding and Genetic Perspectives.* (eds. Ali, J. & Wani, S.H.) 203–220 (Springer International Publishing, 2021).
64. Shah, F. et al. Impact of high-temperature stress on rice plant and its traits related to tolerance. *J. Agric. Sci.* **149**, 545–556 (2011).
65. Simpson, C., Hosking, J. S., Mitchell, D., Betts, R. A. & Shuckburgh, E. Regional disparities and seasonal differences in climate risk to rice labour. *Environ. Res. Lett.* **16**, 124004 (2021).
66. Aghamolki, M. T. K. et al. Heat stress effects on yield parameters of selected rice cultivars at reproductive growth stages. *J. Food Agric. Environ.* **12**, 741–746 (2014).
67. Domeisen, D. I. et al. Prediction and projection of heatwaves. *Nat. Rev. Earth Environ.* **4**, 36–50 (2023).
68. Li, H., Sun, B., Wang, H., Zhou, B. & Duan, M. Mechanisms and physical-empirical prediction model of concurrent heatwaves and droughts in July–August over northeastern China. *J. Hydrol.* **614**, 128535 (2022).
69. Li, J., Zheng, C., Yang, Y., Lu, R. & Zhu, Z. Predictability of spatial distribution of pre-summer extreme precipitation days over southern China revealed by the physical-based empirical model. *Clim. Dynam.* **61**, 2299–2316 (2023).
70. Lyu, Y. et al. Improving subseasonal-to-seasonal prediction of summer extreme precipitation over southern China based on a deep learning method. *Geophys. Res. Lett.* **50**, e2023GL106245 (2023).
71. Lyu, Y. et al. Significant advancement in subseasonal-to-seasonal summer precipitation ensemble forecast skills in China mainland through an innovative hybrid CSG-UNET method. *Environ. Res. Lett.* **19**, 074055 (2024).

72. Dee, D. P. et al. The ERA-Interim reanalysis: configuration and performance of the data assimilation system. *Q. J. R. Meteorol. Soc.* **137**, 553–597 (2011).
73. Menne, M. J., Durre, I., Vose, R. S., Gleason, B. E. & Houston, T. G. An overview of the global historical climatology network-daily database. *J. Atmos. Oceanic Technol.* **29**, 897–910 (2012).
74. Wheeler, M. & Kiladis, G. N. Convectively coupled equatorial waves: analysis of clouds and temperature in the wavenumber–frequency domain. *J. Atmos. Sci.***56**, 374–399 (1999).
75. Kiladis, G. N., Wheeler, M. C., Haertel, P. T., Straub, K. H., & Roundy, P. E. Convectively coupled equatorial waves. *Rev.Geophys.* https://doi.org/10.1029/2008RG00026 (2009).
76. Kiladis, G. N., Straub, K. H. & Haertel, P. T. Zonal and vertical structure of the Madden–Julian oscillation. *J. Atmos. Sci.* **62**, 2790–2809 (2005).
77. Straub, K. H. & Kiladis, G. N. Observations of a convectively coupled Kelvin wave in the eastern Pacific ITCZ. *J. Atmos. Sci.* **59**, 30–53 (2002).
78. Seo, Y. W. & Ha, K. J. Changes in land-atmosphere coupling increase compound drought and heatwaves over northern East Asia. *npj Clim. Atmos. Sci.* **5**, 100 (2022).
79. Guo, W., Wang, X., Sun, J., Ding, A. & Zou, J. Comparison of land–atmosphere interaction at different surface types in the mid-to lower reaches of the Yangtze River valley. *Atmos. Chem. Phys.* **16**, 9875–9890 (2016).
80. Lyu, Y. et al. Subseasonal forecasts of precipitation over maritime continent in boreal summer and the sources of predictability. *Front. Earth Sci.* **10**, 970791 (2022).
81. Zhang, L., Kim, T., Yang, T., Hong, Y. & Zhu, Q. Evaluation of subseasonal-to-seasonal (S2S) precipitation forecast from the North American multi-model ensemble phase II (NMME-2) over the contiguous US. *J. Hydrol.* **603**, 127058 (2021).
82. Stan, C. et al. Advances in the prediction of MJO teleconnections in the S2S forecast systems. *Bull. Am. Meteorol. Soc.* **103**, E1426–E1447 (2022).
83. Dai, G., Mu, M., Li, C., Han, Z. & Wang, L. Evaluation of the forecast performance for extreme cold events in East Asia with subseasonal-to-seasonal data sets from ECMWF. *J. Geophys. Res. Atmos.* **126**, 2020JD033860 (2021).
84. Xie, J., Yu, J., Chen, H. & Hsu, P. C. Sources of subseasonal prediction skill for heatwaves over the Yangtze River Basin revealed from three S2S models. *Adv. Atmos. Sci.* **37**, 1435–1450 (2020).
85. Leach, N. J., Weisheimer, A., Allen, M. R. & Palmer, T. Forecast-based attribution of a winter heatwave within the limit of predictability. *Proc. Natl Acad. Sci. USA* **118**, e2112087118 (2021).

Acknowledgements

This research was supported by various grants from the Ministry of Education of Singapore (#Tier1 RG74/22, #Tier2 MOET2EP10121-0008, and #Tier3 MOET32022-0006). Y.W. was supported by National Research Foundation, Prime Minister's Office, Singapore, and National University of Singapore (NUS) under Sustainable Tropical Data Centre Test bed program (STDCT); Agency for Science, Technology and Research (A*STAR) under Cognitive Digital Twin and Physics-based ML for Battery Analytics program (M23L9b0052). This work comprises EOS contribution number 611.

Author contributions

Y.L. and J.W.: formal analysis, writing—original draft and editing, visualization. J.W., X.Z. and X.W.: conceptualization, J.W., X.Z., H.Z. and Y.W.: supervision, funding acquisition, writing—review and editing. E.P., J.L., X.Wan, S.Z. and D.D.T.: writing—review and editing.

Competing interests

The authors declare no competing interests.

Additional information

Supplementary information The online version contains supplementary material available at https://doi.org/10.1038/s41612-024-00797-w.

Correspondence and requests for materials should be addressed to Jingyu Wang or Xiefei Zhi.

Reprints and permissions information is available at http://www.nature.com/reprints